RESEARCH ARTICLE | MAY 10 2021

A real-time flow forecasting with deep convolutional generative adversarial network: Application to flooding event in Denmark

Meiling Cheng (程美玲) [iD] ; Fangxin Fang (方芳欣) ✉ [iD] ; I. M. Navon [iD] ; C. C. Pain
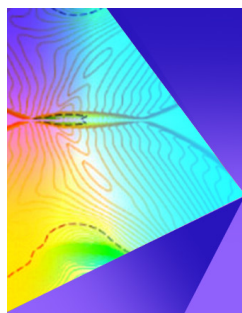
Check for updates

CrossMark

View Online

Export Citation

Physics of Fluids

Special Topic: Shock Waves

Submit Today!

AIP Publishing

A real-time flow forecasting with deep convolutional generative adversarial network: Application to flooding event in Denmark

View Online   Export Citation   CrossMark

Meiling Cheng (程美玲),[1] [iD] Fangxin Fang (方芳欣),[1,a] [iD] I. M. Navon,[2] [iD] and C. C. Pain[1]

AFFILIATIONS

[1]Applied Modelling and Computation Group, Department of Earth Science and Engineering, Imperial College London, London SW7 2BP, United Kingdom
[2]Department of Scientific Computing, Florida State University, Tallahassee, Florida 32306-4120, USA

[a]Author to whom correspondence should be addressed: f.fang@imperial.ac.uk

ABSTRACT

Real-time flood forecasting is crucial for supporting emergency responses to inundation-prone regions. Due to uncertainties in the future (e.g., meteorological conditions and model parameter inputs), it is challenging to make accurate forecasts of spatiotemporal floods. In this paper, a real-time predictive deep convolutional generative adversarial network (DCGAN) is developed for flooding forecasting. The proposed methodology consists of a two-stage process: (1) dynamic flow learning and (2) real-time forecasting. In dynamic flow learning, the deep convolutional neural networks are trained to capture the underlying flow patterns of spatiotemporal flow fields. In real-time forecasting, the DCGAN adopts a cascade predictive procedure. The last one-time step-ahead forecast from the DCGAN can act as a new input for the next time step-ahead forecast, which forms a long lead-time forecast in a recursive way. The model capability is assessed using a 100-year return period extreme flood event occurred in Greve, Denmark. The results indicate that the predictive fluid flows from the DCGAN and the high fidelity model are in a good agreement (the correlation coefficient $\geq 97\%$ and the mean absolute error ≤ 0.008 m) for a lead-900 time step forecast. This is an important step toward real-time flow forecasting although further evaluation of the DCGAN performance is required in complex realistic cases in the future.

NOMENCLATURE

p_r Total number of nodes in a scalar grid in the computation domain Ω

X Locations of nodes in the computation domain Ω, $X = (X_1, \ldots, X_{p_z}, \ldots, X_{p_r})$

τ Lead time length of the predictive variable solutions

K Previous time length of the historical variable solutions

U Variable solutions at temporal and spatial spaces

$\tilde{U}$ Variable forecast during the lead time period $t_N, t_{N+\tau}$

U_g Variable solutions obtained by the generator during the training process

U_d Real variable data used to distinguish it from the generated data U_g during the training process

I Input dataset, containing previous length-K time series of variable solutions

O Output dataset, containing the one-time step-ahead predictive variable solution

I. INTRODUCTION

Floods, as one of the most dangerous natural disasters, cause loss of life and property in many countries in the world. For example, according to a report by the Parliamentary Office of Science and Technology,[1] urban flooding causes losses of 270 million pounds per year in England and Wales with 80 000 homes at risk. Therefore, rapid real-time flood forecasting is of great significance for flood hazard mitigation and advanced management of policy responses to flood disaster.[2–4] In general, floods are characterized by nonlinearity and non-stationarity fluid flows,[5–7] which exhibit complex spatiotemporal dynamics. In addition, the long lead-time flood forecasting faces the increasing uncertainties from various sources, for example, model inputs and parameters. Thus, it is particularly difficult to make accurate long lead-time flood forecast in traditional computational dynamic models.[8]

Recent research progress reports have demonstrated that machine learning-based methods are powerful in simulating nonlinear

and complex systems.[9–11] The deep learning methods can identify the main dynamic patterns from historical datasets and reveal the intricate structures.[12–17] Recent research efforts in machine learning have been made to predict the spatiotemporal physical dynamics.[14,18–20] For example, Hu *et al.*[18] proposed a long-short term memory (LSTM)-reduced order model (ROM) for flooding prediction, where having the compatibility of LSTM and ROM enabled solving predictive problems efficiently and accurately. Ahmed *et al.*[21] And Shi *et al.*[22] first introduced convolutional neural network (CNN) to LSTM for precipitation now-casting. It has been proved that CNN is a powerful tool for extracting the spatial dynamic features and reducing the dimensional size. Wiewel, Becher, and Thuerey[14] also proposed the hybrid-CNN-LSTM for predicting the temporal evolution of dense physical functions. Notwithstanding the success of machine learning in the aforementioned applications, most of these models are applicable to sequence nowcasting using the history datasets, and only one-time step-ahead or very short lead-time forecast could be achieved.[23–27] There are still challenges in real-time forecasting for a long lead-time, for example,

- *Uncertainty in future flow dynamics (meteorological, hydrological and boundary condition uncertainty):* we need to explore whether the trained machine learning model using the datasets in the past is able to predict the future flow dynamics (beyond the training period). This is dependent on whether the available training datasets are good/big enough for capturing various complex fluid flow dynamics in the future.
- *Accumulated forecast error:* In real-time forecasting, the predicted variable solution from the previous time levels will be used as inputs for prediction at the next time levels. With increasing the length of forecast, the cumulative error in time series prediction may become larger, thus leading to a predictive failure in long lead-time forecasting. In the work of Hu *et al.*,[18] it was found that the predictive accuracy in LSTM modeling decayed rapidly when the predictive lead-time was extended to beyond the training period. This indicates that capturing dependencies of features between successive time periods in the model becomes more intractable as the prediction horizon extends in time. This constitutes a challenge in real-time forecasting for a long lead-time.

In this work, a deep convolutional generative adversarial network (DCGAN) is proposed to tackle challenges presented by the long lead-time flooding forecasting. GANs are capable of processing high-dimensional datasets and producing high-resolution images.[28–31] Recent progress in deep learning has shown that GAN-based techniques are promising for spatiotemporal-based applications such as trajectory prediction, events generation and time-series data imputation.[32] Cheng *et al.*[33] first introduced DCGAN for predicting spatiotemporal flow distributions. This work mainly focused on simulations of parameterized nonlinear fluid flows for a training period. It was shown that the complex features of flow dynamics were captured by the adversarial networks.

In this work, further implementation of the DCGAN has been presented for long lead-time flood forecasting in the future (beyond the trained period). The capability of the DCGAN has been evaluated for a realistic flooding event in Denmark. The main features of the predictive DCGAN are:

- An efficient DCGAN architecture, consisting of deep convolutional neural networks, learns rich distributions from the high-

dimensional spatiotemporal datasets and yields a low computation cost for predicting spatiotemporal floods.
- A cascade predictive implementation of the DCGAN provides accurate predictive results for a long lead-time, which highlights the potential in complex and massive applications. During dynamic flow learning, the spatiotemporal flow features of historical high-dimensional flow fields are deeply exploited by the deep convolutional neural networks, thus capturing the underlying flow patterns. During real-time forecasting, the forecast process follows a cascade manner, which means that the last one-time step-ahead predictive solution is used as a new input for the next step forecast.
- Having the capability of exploring the flood propagation process over an urban area.

The paper is organized as follows: The governing equations for flood forecast problems are briefly formulated in Sec. II. The real-time DCGAN for flood forecasting is introduced in detail in Sec. III. Section IV demonstrates the predictive performance of the DCGAN using flood events in Greve, Denmark, as a realistic test case. Finally in Sec. V, conclusions are presented.

II. SPATIOTEMPORAL FLOOD FORECASTING PROBLEM

In traditional computational dynamic models, the parameterized set of partial differential equations (for example, the Navier–Stokes or shallow water equations) are used for resolving flood dynamics problems as

$$R(U, \mu, x, t) = S, \tag{1}$$

where R is the nonlinear model operator, U represents the variables to be predicted (for example, velocity, pressure, water depth, etc.), x is the spatial coordinate system, μ denotes the uncertainty parameters, boundary and initial conditions, t is the time, and S denotes the source term.

The spatiotemporal flood forecast process is a way to learn from the historical dataset $U \in \Re^{t_N \times p_r}$ and predict the future flow solution $U \in \Re^{t_{N+\tau} \times p_r}$ on the spatial space (where τ is the lead time step, N represents the number of time steps, p_r is the total number of nodes in the computation domain Ω). Given the solutions/dataset at the previous length-K time series of variable solutions $\{U_{t_i} | i = 1, \ldots, K\}$, the forecast of length-τ time series of variable solutions $\{U_{t_i} | i = 1, \ldots, \tau\}$ can be expressed mathematically as

$$U_{t_{n+1}}, \ldots, U_{t_{n+\tau}} = P(U_{t_{n-K+1}}, \ldots, U_{t_n}, \mu), \tag{2}$$

where P represents a dynamic forecast model for the fluid flows expressed in Eq. (1), U_{t_n} is the variable spatial solution at time step t_n, and μ as the conditional input is used to improve the forecast accuracy. In this work, the dynamic predictive model P will be represented by a real-time predictive DCGAN, which will be introduced in Sec. III.

The variables used in Secs. III and IV are defined in the Nomenclature.

III. DEEP CONVOLUTIONAL GAN FOR REAL-TIME FLOOD FORECASTING

The main objective of this work is to develop a real-time predictive DCGAN tool for spatiotemporal flood modeling. To achieve this objective, a two-stage process is adopted (shown in Fig. 1):
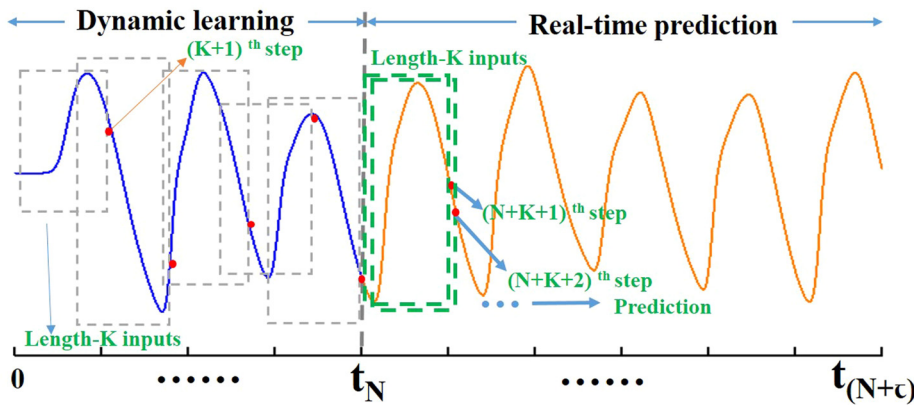
- *Dynamic flow learning.* During the training process, the dynamic model P in Eq. (2) is represented by the DCGAN, which combines the generator G and discriminator D modules. Given the training input–output datasets (I^{tr}, O^{tr}), the spatiotemporal flow features and dynamic patterns of historical floods are deeply exploited by the DCGAN. Once the training process is finished, an optimal dynamic system P is obtained aiming to learn the flow features in time and space (the details of the training process, see Sec. III A).
- *Real-time forecasting.* The real-time forecast adopts a cascade manner for predicting the flow evolution over time. The last one-time step-ahead forecast from the DCGAN can act as a new input for the one-time step-ahead forecast, which forms a long lead-time forecast in a recursive way (the details of the forecasting process, see Sec. III B).

A. Dynamic flow learning of DCGAN

A DCGAN consists of two modules: a generator G and a discriminator D.[34] As shown in Fig. 2, the generator is responsible for generating spatiotemporal distributions of data U_g from a random distribution I. The discriminator is responsible for distinguishing the real data U_d from the generated data U_g by making a binary decision. Therefore, the dynamic model P is represented by the two modules in the DCGAN ($P = (G, D)$).

1. Generator network

We use a deep neural network F_g that takes the inputs I with length-K time steps $\{U_{t_{n-K+1}}(X), \ldots, U_{t_{n-i+1}}(X), \ldots, U_{t_n}(X), \mu\}$. As shown in Fig. 2, the generator consists of deep convolutional layers, and each hidden layer is followed by an activation function [e.g., the rectifier nonlinearity (ReLU), the hyperbolic tangent function, and the sigmoid function].[35] The convolutional layers are able to capture the spatial and temporal dependencies in a flood field by using filters. Filters often extract certain types of features from the inputs and can represent spatially localized interactions.[36] The batch normalization[37] is used which stabilizes learning by normalizing the output values retain a mean of 0 and standard deviation of 1. During the training process shown in Fig. 2, the parameters ψ (weights and bias in the

neural network) in the generator are updated to minimize the loss function $\mathscr{L}_G$,

$$\mathscr{L}_G = E_{I \sim p_I(I)}[\log(1 - D(G(I)))], \tag{3}$$

where $p_I(I)$ is a prior distribution for the inputs I.

2. Discriminator network

The discriminator takes as its inputs a generated forecast U_g and a targeted output (i.e., real data) O ($O = U_d = U_{t_{n+1}}(X)$). The generated and targeted datasets in the discriminator are processed using deep convolutional layers and full-connected layers, and each hidden layer is also followed by an activation function and batch normalization similar to the architecture used in the generator. The output layer is densely connected to the final hidden layer which yields a number between 0 and 1. The output $D(U_d) = 1$ means that the targeted outputs U_d are accepted by the discriminator while $D(G(I)) = 0$ means that the generated forecasts U_g are rejected.

In the model training process, the parameters ζ (weights and bias in the neural network) in the discriminator are updated by maximizing $\mathscr{L}_D$ as

$$\mathscr{L}_D = E_{U_d \sim p_{data}(U_d)}[\log D(U_d)] + E_{I \sim p_I(I)}[\log(1 - D(G(I)))], \tag{4}$$

where $p_{data}(U_d)$ is the probability data distribution for the targeted outputs U_d.

Combining the loss functions $\mathscr{L}_G$ in Eq. (3) and $\mathscr{L}_D$ in Eq. (4), the objective function for the DCGAN can be expressed as

$$\min_G \max_D \mathscr{L}(G, D) = E_{U_d \sim p_{data}(U_d)}[\log D(U_d)] \\ + E_{I \sim p_I(I)}[\log(1 - D(G(I)))]. \tag{5}$$

In practice, gradient-based methods, for example, the adaptive moment estimation (Adam) optimizer[38] and RMSprop,[39] are used to optimize the loss function $\mathscr{L}(G, D)$. The model architecture and parameters of the DCGAN are described in detail in Table I applied to flood prediction problems in this paper. After completing the dynamic learning process of the DCGAN, the parameters in the generator and discriminator are optimized. The flood fields U in the lead-time steps can then be predicted by the DCGAN.
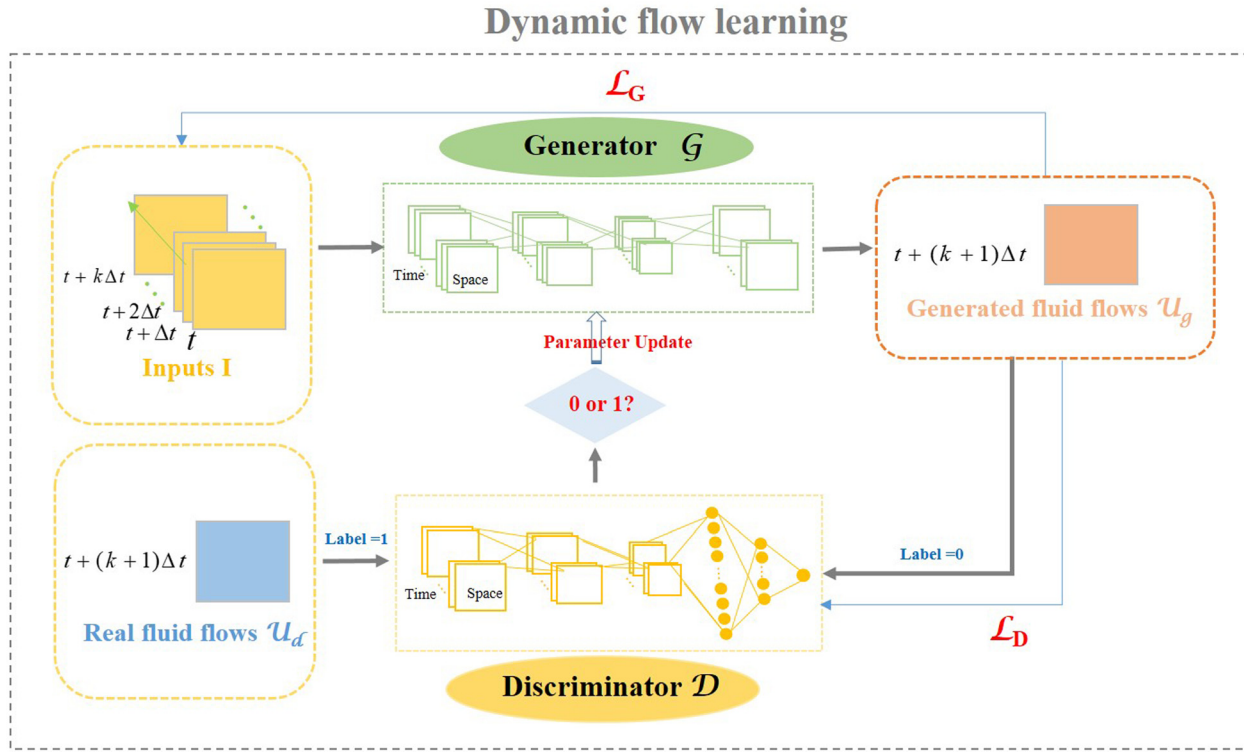
FIG. 2. Illustration of the dynamic flow learning system: a deep convolutional GAN (DCGAN), which consists of a generator and a discriminator. The generator and discriminator are composed of convolutional layers and full-connected layers. The combination of the loss functions in two modules forms the adversarial training.

TABLE I. Architecture and model parameter setting of the DCGAN.

Module	Layer
Generator G	Input
	Conv2D, leaky ReLU ($\alpha = 0.2$)
	Conv2D, leaky ReLU ($\alpha = 0.2$)
	Conv2D, leaky ReLU ($\alpha = 0.2$)
	Conv2D, leaky ReLU ($\alpha = 0.2$)
	Output, Tanh
Discriminator D	Input
	Conv2D, leaky ReLU ($\alpha = 0.2$)
	Conv2D, leaky ReLU ($\alpha = 0.2$)
	Conv2D, leaky ReLU ($\alpha = 0.2$)
	Conv2D, leaky ReLU ($\alpha = 0.2$)
	Full connected, leaky ReLU ($\alpha = 0.2$)
	Output (1), Sigmoid
Parameters	Setting
Filter size	3×3
Batch normalization	momentum $= 0.8$
Batch size	10
Optimizer	Adam
Learning rate; momentum	2×10^{-4}, 0.5
Epochs	500

B. Real-time forecast of DCGAN

Once the DCGAN used for representing the dynamic model P is generated during the dynamic learning process, the one-time step-ahead forecast of fluid field $\tilde{U}$ can be obtained. For the one-time step-ahead flood forecast in Eq. (2) can be rewritten as

$$U_{t_{n+1}}(X) = G\big(U_{t_{n-K+1}}(X), ..., U_{t_n}(X), \mu\big). \qquad (6)$$

To further achieve the long lead-time forecast of floods, a cascading deployment is used as shown in Fig. 3. It starts with the one-time step-ahead forecast $\{\tilde{U}_{t_n}(X)|n = K + 1\}$, given the inputs $I \in \Re^{t_K \times p_r}$ containing $K -$ time steps historical data $\{U_{t_n}(X)|n = 1, .., K\}$. Afterwards, in the following one-time step-ahead forecast $\{\tilde{U}_{t_n}(X)|n = K + 2, ...\}$, the previous predicted solution $\{\tilde{U}_{t_n}(X)|n = K + 1, ...\}$ will be included in the inputs. Given the previous length-K time steps, the forecast of length-τ time steps in Eq. (2) or Eq. (6) can be rewritten as

$$\tilde{U}_{t_{n+i}}(X)$$
$$= \begin{cases} G\big(U_{t_{n-k+i}}(X), ..., U_{t_n}(X), \tilde{U}_{t_{n+1}}(X), ..., \tilde{U}_{t_{n+i-1}}(X), \mu\big), & i \leq K, \\ G\big(\tilde{U}_{t_{n-K+i}}(X), ..., \tilde{U}_{t_{n+i-2}}(X), \tilde{U}_{t_{n+i-1}}(X), \mu\big), & i > K, \end{cases}$$
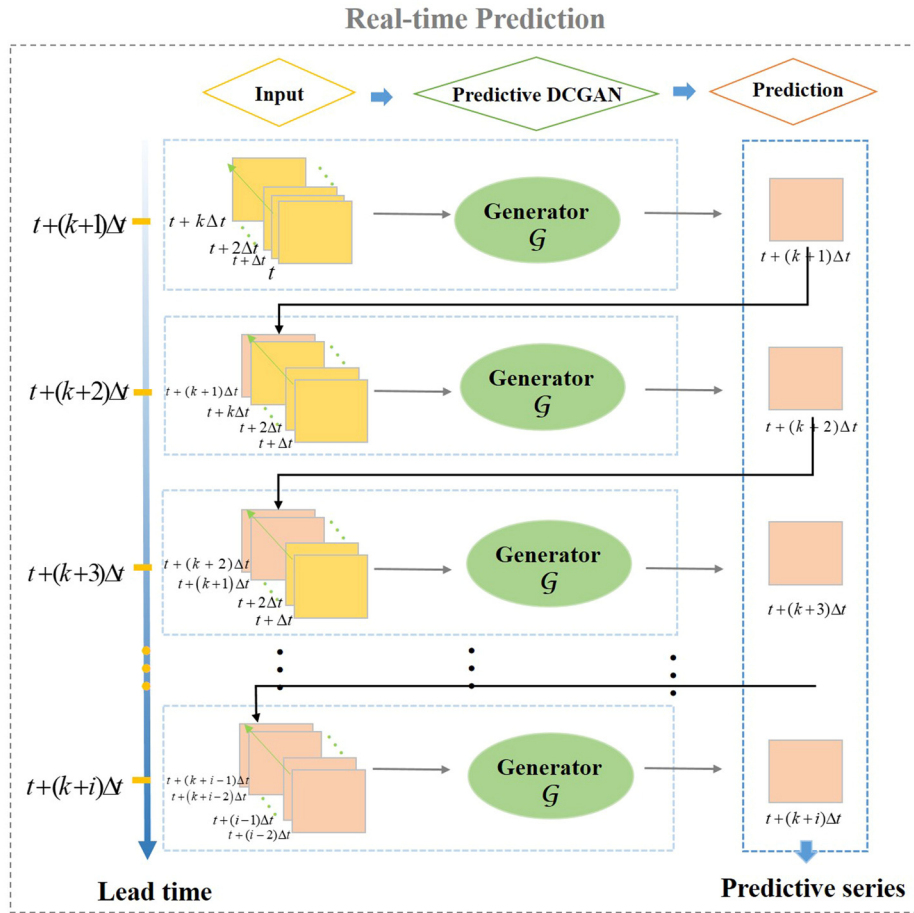$$(7)$$

Real-time Prediction

FIG. 3. Illustration of the real-time forecast of the DCGAN. The forecast of flood fields employs a cascade manner, i.e., the last one-time step-ahead forecast from the DCGAN can act as a new input for the next step-ahead forecast, which forms a long lead-time forecast in a recursive way.

where $i = (1, \ldots, \tau)$, and the historical flow datasets $(U_{t_{n-k+i}}, \ldots, U_{t_n}(X))$ are used when $i < K$, while all the inputs originate from the predicted solution at the previous time steps when $i > K$ (beyond the training period).

C. Model evaluation

To assess the performance of the DCGAN model developed in this study, different statistical evaluations including the root mean squared error (RMSE), the Nash–Sutcliffe efficiency coefficient (NSE), the coefficient of correlation (CC), the mean absolute error (MAE), the mean magnitude of relative error (MMRE), Nash–Sutcliffe efficiency ratio (NSER), and the percentage of accuracy-precision (PAP)[40] are used. The Nash–Sutcliffe efficiency coefficient and percentage of accuracy-precision are defined as

$$NSE = 1 - \left[\frac{\sum_{i=1}^{n} (U_g^i - U_d^i)^2}{\sum_{i=1}^{n} (U_d^i - \overline{U_d^i})^2} \right], \quad (8)$$

$$PAP = 100 \left(1 - \frac{\sqrt{2}}{2} \sqrt{ \left(\frac{1}{n} \sum_{i=1}^{n} \left| \frac{U_g^i - U_d^i}{U_d^i} \right| \right)^2 + \left[\frac{\sum_{i=1}^{n} (U_g^i - U_d^i)^2}{\sum_{i=1}^{n} (U_d^i - \overline{U_d^i})^2} \right]^2 } \right), \quad (9)$$

where U_g^i and U_d^i are the ith forecasting and observed flows, respectively, and $\overline{U_d}$ is the average observed flow. The MMRE and NSER vary between 0 and $+\infty$, with acceptable levels of performance between 0 and 1. The PAP ranges from 0 to 100, while zero indicates both poor accuracy and precision.[40]

The forecasts are also analyzed in terms of their distributions by using the Q–Q plot, which is a visual method comparing the values of observations in the predictive distribution on the x-axis and the uniform distribution on the y-axis to examine the reliability of the forecasting distribution. If the plot follows a 1:1 line, it means that the flood forecasts are perfectly reliable. The advantage of Q–Q plot is that it can illustrate different aspects of forecasts including under- or over-estimated predictive uncertainty.[41]
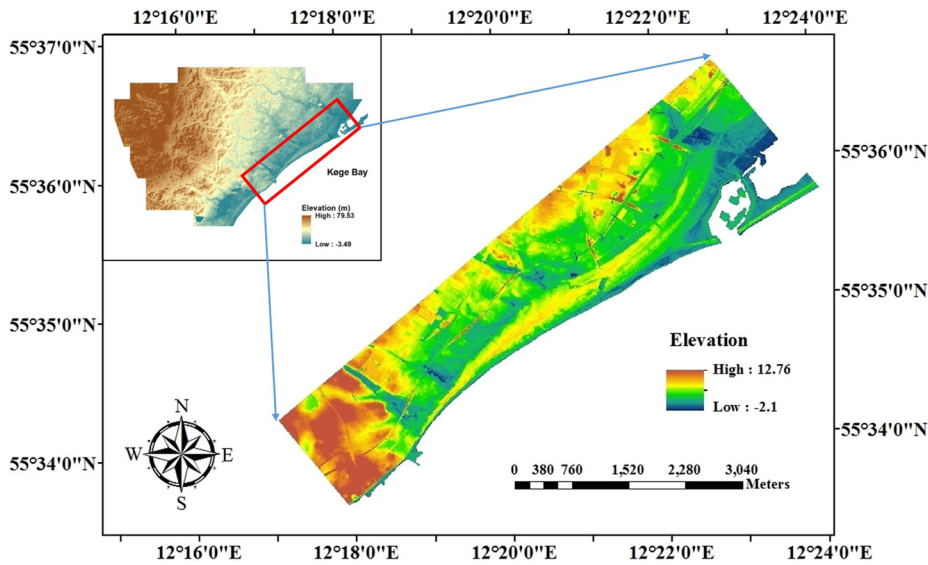
FIG. 4. Study area in Greve, Municipality of Denmark (left side see Ref. 43).

IV. APPLICATION AND RESULTS

A. Study area

To assess the long lead-time predictive capability of the DCGAN model, it has been applied to a flood event in the northeastern part of Greve, Denmark. As shown in Fig. 4, Greve is a coastal city connected to the Baltic Sea, with elevations between 12.76 and −2.1 m in the study domain area. It is potentially affected by flood disasters induced by extreme sea-level events along its coast. For example, an extreme historical flood in Køge Bay occurred in 13th October 1760, with a maximum water level of 3.7m.[42] Considering the impact of climate change in the next 100 years, future climate change conditions should be taken into account to estimate the future extreme sea-level.[43] Therefore, a 100-yr return period extreme water level event (2100

upper sea-level flood event in Berbel and Roman[42]) was used in this paper, to predict the expected changes in future sea surges (as shown in Fig. 5).

In this study, the training datasets and reference solutions (referred to as the real/original water depths) are obtained from the simulation results by running the high fidelity model—MIKE 3 FM, which is a software tool for modeling unsteady three-dimensional free surface flows.[44] As shown in Fig. 5, the model domain representing the coastal area in Greve (Denmark) has a size of 2.3×7.5 km. The unstructured mesh consists of a total of 39 290 points. An extreme sea-water level event with a maximum value 3.08 m is used as the input boundary condition along the coastal line. No normal flow boundary conditions were applied to other boundaries. The total simulation time was 24h with a time step $\Delta t = 1$ s. The simulations started from
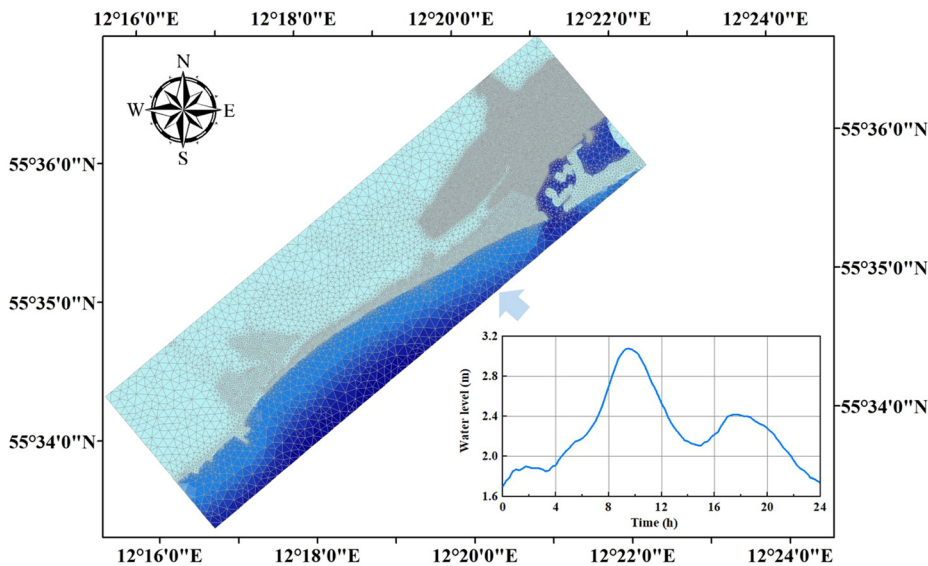

FIG. 5. Unstructured mesh of study area and extreme sea water level along the coastal line.

a "static" state. To illustrate the DCGAN capability for uncertainty analysis and forecast, Sec. IV A performs a sensitivity analysis by the DCGAN with respect to different incoming waves along the coastline, while Sec. IV B demonstrates the forecasting capability of the DCGAN for a long lead-time.

B. Uncertainty quantification

In this section, to evaluate model uncertainty in spatiotemporal flood modeling, we consider different flood events of observed and predicted floods using different incoming waves. As shown in Fig. 5, 15 types of input parameters (incoming waves) range from -30% to $+30\%$ of the water level in 2100 upper sea-level flood event are generated using a Gaussian distribution $N(\bar{\mu}, \sigma^2)$. For example, the mean $\bar{\mu}$ is 2.18 m and the variance of the distribution σ^2 is 0.047 m at $t = 6$ h in Fig. 6(b). At $t = 12.5$ h in Fig. 6(c), the water levels in 15 types of incoming waves are obtained from the Gaussian distribution between 1.632 and 3.147 m.

Given a set of incoming waves (in Fig. 6), the corresponding solution snapshots U (a total of 145 snapshots sampled at an equal time interval of $\Delta t = 10$ min from 0 to 24 h, $N = 145, p_r = 39\,290$) are obtained by running the high fidelity model. In model training and validation processes, a predictive DCGAN is constructed by using the training and validated input-output pairs. We use the first 12 types of incoming waves as the training inputs I^{tr}, while the corresponding training outputs O^{tr} are the collection of the solution snapshots for each type of incoming waves. During the online predictive process, given a set of new inputs I^{pre}, the predictive analysis is undertaken by

the DCGAN. Here, the inputs I^{pre} are the last three types of incoming waves (wave 13–15) shown in Fig. 6.

For a given input $\mu \in I^{pre}$ (wave 13), Fig. 7 presents the comparison of water depth obtained from the DCGAN and the original high fidelity model at $t = 5, 9, 14, 18$ h. It is worth noting that the predicted flow fields from the DCGAN attain a closer agreement with those from the high fidelity model at different time levels. The basic flow physics is clearly captured, and the shape of the water depth is predicted quite well, especially in urban areas (as shown in the rectangles in Fig. 7). In addition, a relatively good correspondence is observed between the predicted depth of DCGAN and those of the original high fidelity model: the correlation coefficient of results at time levels $t = 5, 9, 14, 18$ h achieves values beyond 97% shown in Fig. 8. Table II further summarizes the statistical metrics for model performance. It can be seen that the values of MMRE and NSER at different time levels are below 0.25, and the PAP values are beyond 82.

The results indicate that the DCGAN is able to obtain accurate simulations of spatiotemporal distribution during a fixed simulation period for given varied boundary conditions. The spatiotemporal flow features have been faithfully represented as the flow evolves, and the magnitude of predicted water depth during the simulation period is in a good agreement with the reference water depth. The promising results obtained show that the DCGAN is able to detect the underlying functional mapping through pattern extraction, confirming results obtained in the work of.[35,45,46] Leinonen, Guillaume, and Yuan[45] suggested that the DCGAN has potential to solve probability distribution problems in which the random fields have complex spatial structures.
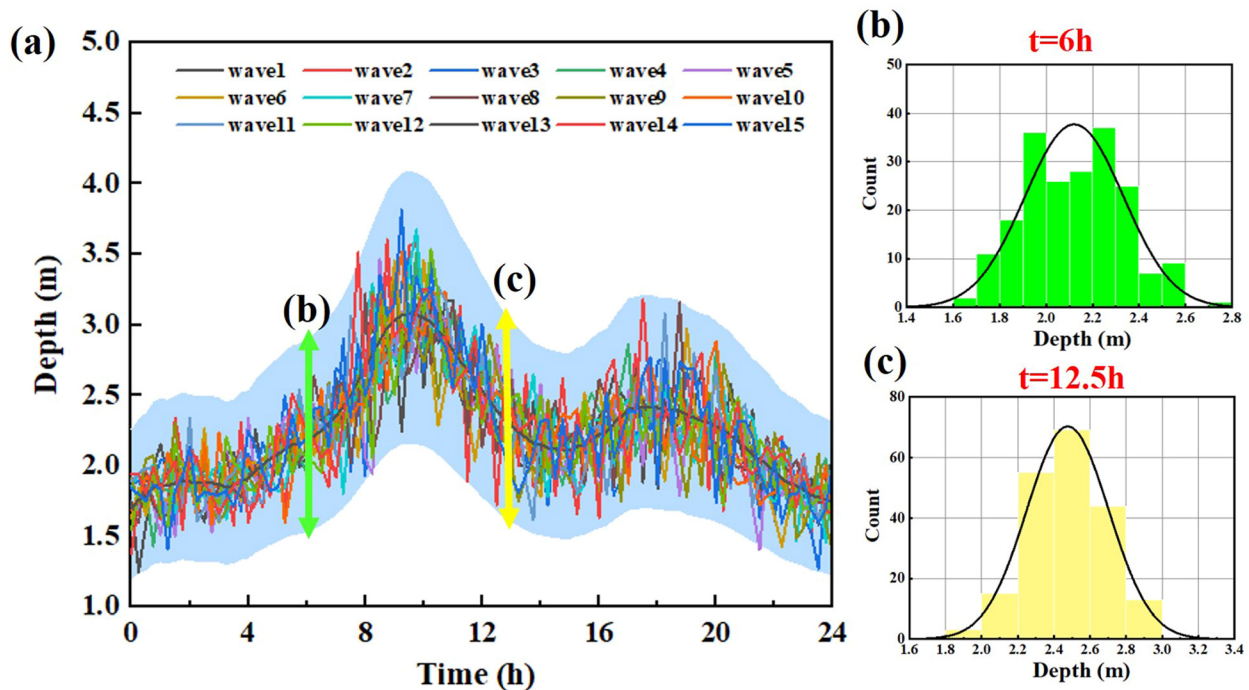
FIG. 6. Different types of incoming waves obtained from the Gaussian distribution of the extreme sea water level (the solid line representing the 2100 upper sea flood level in Fig. 5) from 0 to 24 h. (a) represents 15 types of incoming waves, and (b) and (c) are the Gaussian distribution of water depths at $t = 6$ and 12.5h, respectively.
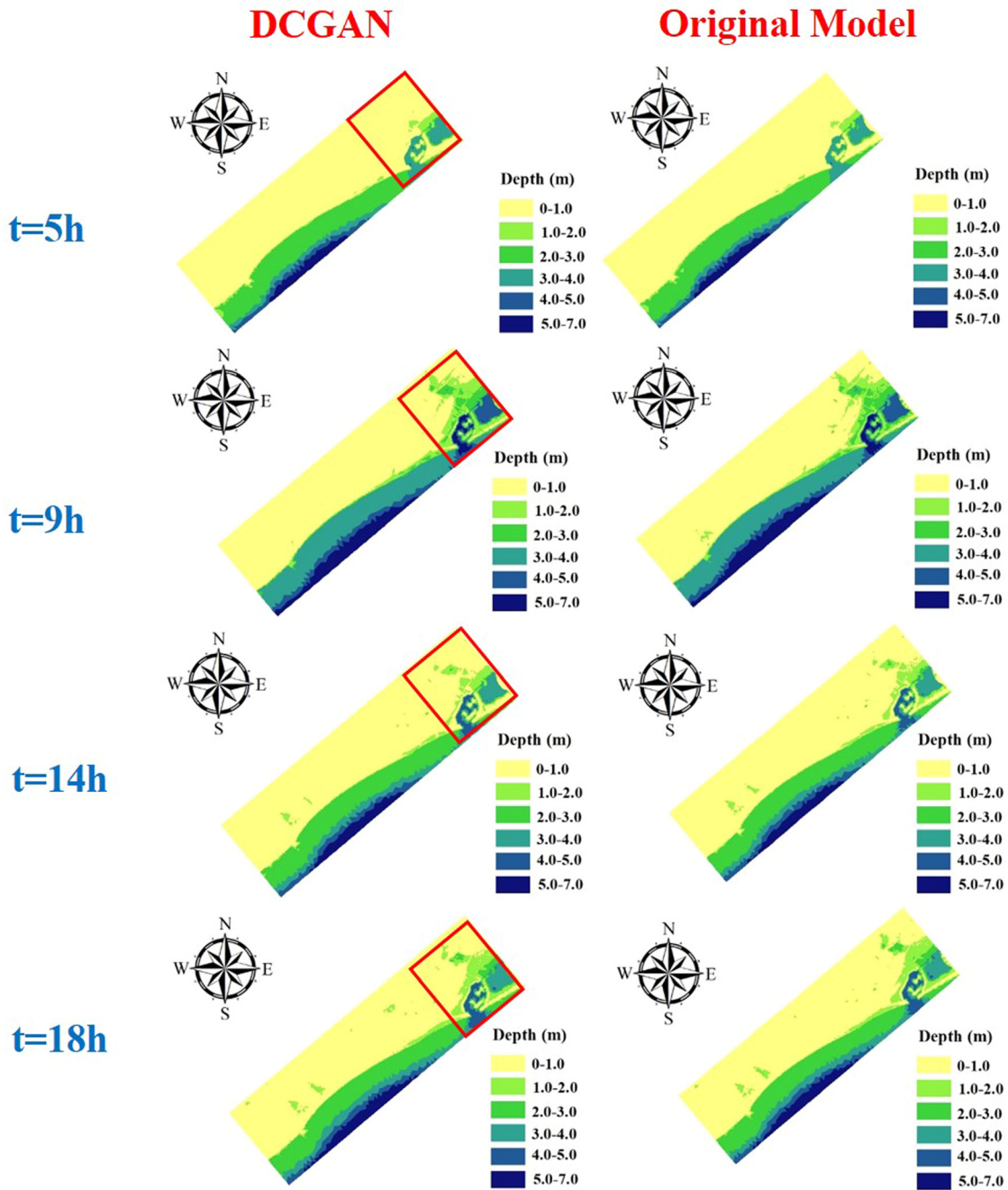
FIG. 7. Comparison of the spatial distribution of predictive water depth obtained from the DCGAN and the original high fidelity model at $t = 5, 8, 14, 18$ h.

C. Real-time flooding forecast

In this section, we further test the forecasting ability of DCGAN in future events that is beyond the training time. In this case, given the incoming waves (2100 upper sea-level flood event shown in Fig. 5),

the corresponding solution snapshots U (a total of 2881 snapshots sampled at an equal time interval of $\Delta t = 30$ s from 0 to 24 h) are obtained by running the high fidelity model. In the study scenario, the solutions at first 1800 time steps from 0 s to 15 h are selected as the training datasets, while the remaining datasets from $t_{1801} = 15.01$ to
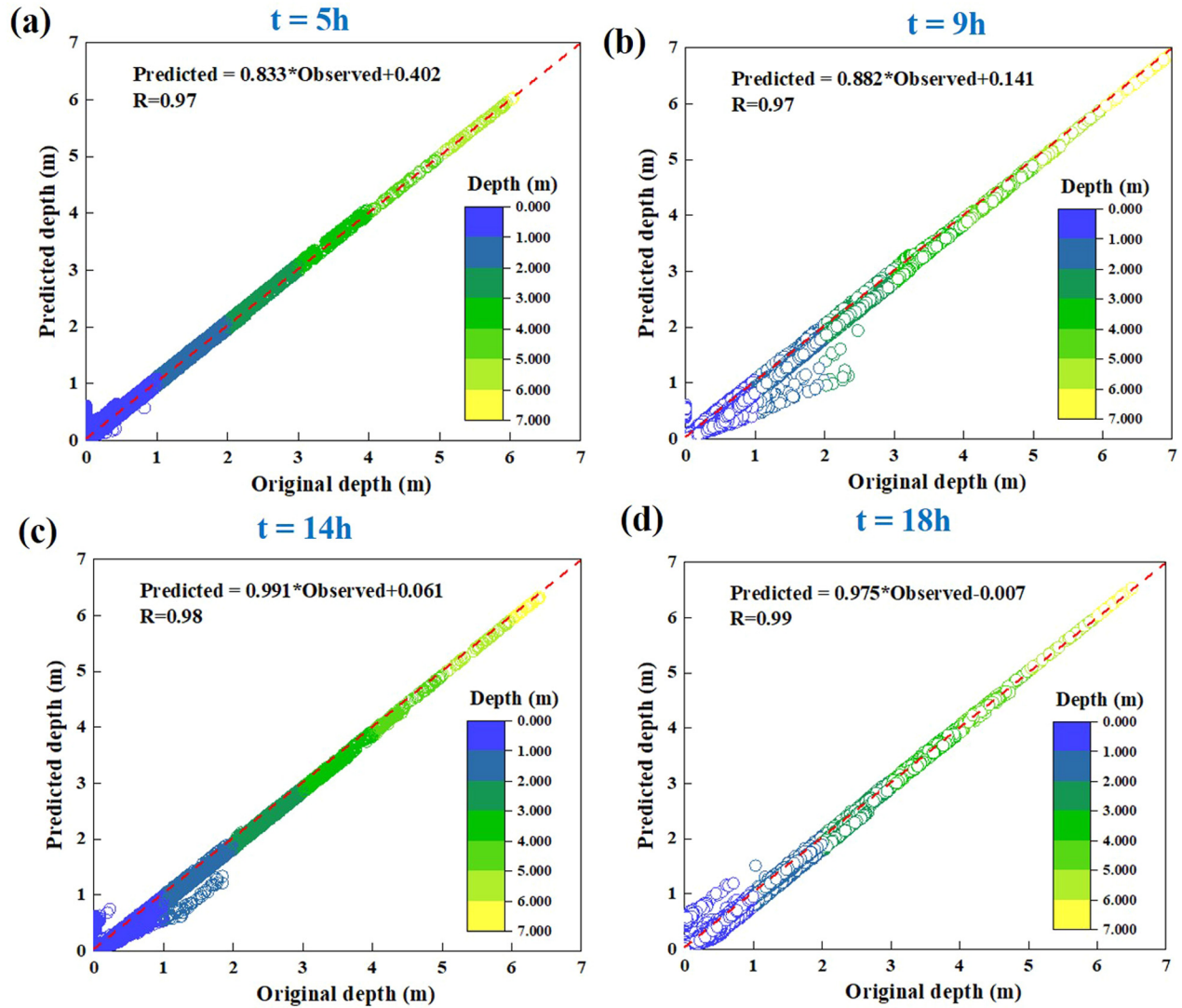
FIG. 8. The correlation coefficients of water depth solutions between the DCGAN and the original high fidelity model at different time levels: (a) $t = 5$, (b) $t = 8$, (c) $t = 14$, and (d) $t = 18$ h.

$t_{2881} = 24$h are prepared for one-time step-ahead forecast (as shown in Fig. 1, $t_N = t_{1800}$ and $t_{N+\tau} = t_{2700}$).

To evaluate the predictive ability of the DCGAN, a comparison between the predicted water depth of the DCGAN and the high

TABLE II. Statistical metrics for water depth solutions between the DCGAN and the original high fidelity model at $t = 5, 8, 14, 18$h.

Time (h)	CC	MMRE	NSER	PAP
$t = 5$	0.97	0.06	0.24	82.5
$t = 8$	0.97	0.14	0.05	89.4
$t = 14$	0.98	0.09	0.04	93
$t = 18$	0.99	0.21	0.01	85.1

fidelity model has been undertaken. Figure 9 depicts the temporal variations of the water depth at eight points within the computational domain area Ω. It can be observed that a relatively good agreement exists between the predictive and original water depths from $t = 15.02$ to $t = 23$ h. The water depths at eight detectors have the same variation tendency as the incoming waves from $t = 15.02$ to $t = 23$ h in Fig. 5. The DCGAN results of the water depth at detectors P5 and P6 along the coastline are very close to those from the high fidelity model although minor differences (< 0.005 m) between results at peaks are noticed. It can be seen that the water depths at detector P1 obtained from the DCGAN have a slight difference from that of original high fidelity model after $t = 21$ h. This is due to the fact that the detector P1 is located at the channel, thus having a larger water depth even though the level of incoming wave reduces. In addition, there
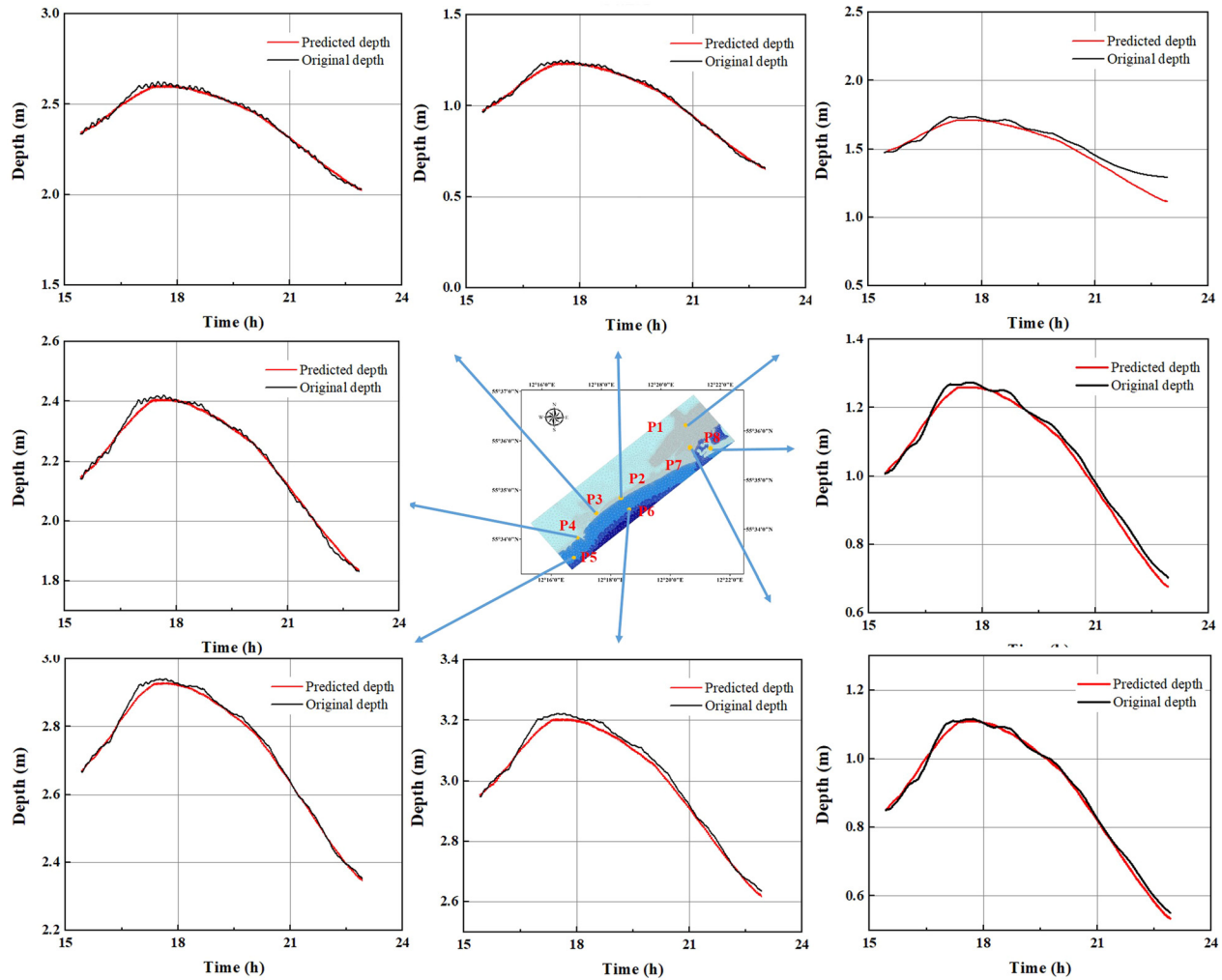
FIG. 9. Comparison of the temporal distribution of predictive water depth obtained from the DCGAN and the original high fidelity model at eight observed points, where the water depth from the high fidelity model is taken as the real (original) depth while the predictive depth is referred to as the results from the DCGAN.

may exist an arrival time lag at detectors if the impact of buildings is taken into account in the flooding simulations.[43] The promising results obtained show that the proposed DCGAN can predict the time series of floods reasonably well in comparison with the high fidelity model.

To depict the spatial distribution of nonlinear fluid fields during the forecasting period (from 15.01 to 23 h), the areas marked with rectangles in Fig. 7 are selected to show the visible changes as the flood propagates over the urban area. The spatial distribution of the predicted water depth at time $t = 15.5, 17.9, 22.8$ h is shown in Fig. 10. Again, very little difference between the results from the DCGAN and the original high fidelity model can be visually noticed at these time steps. The underlying flow pattern is captured well by the predictive DCGAN, especially in complex topographic features, including buildings and channels. The absolute error of the water depth predicted by the DCGAN is also illustrated in Fig. 10, in which the high fidelity model is taken as the reference solution. It can be noticed that most of the

absolute errors are smaller than 0.01 m over the whole domain area at time steps $t = 15.5, 17.9, 22.8$ h. The influence of buildings is observed that the absolute errors increase around buildings when the incoming wave rises from $t = 15.5$ to 17.9 h. However, it relieves when the water depth declines from $t = 17.9$ to 22.8 h.

To further demonstrate the forecasting capability of the DCGAN, the error analysis is carried out by four indicators, i.e., root mean squared error (RMSE), Nash–Sutcliffe efficiency coefficient (NSE), coefficient of correlation (R), and mean absolute error (MAE), for a long lead-time forecast. The corresponding evaluation of forecasting nonlinear flow results during the lead-times from 15.01 to 23 h is illustrated in Fig. 11. It can be seen that the values of RMSE and MAE range from 0 to 0.15 and 0 to 0.08, respectively [in Figs. 11(a) and 11(c)]. It is worth to mention that values of NSE and R are beyond 0.97 and 0.98, respectively [in Figs. 11(b) and 11(d)]. The maximum values of RMSE and MAE, as well as the minimum values of NSE and R, occur when the water level of incoming wave attains its peak around
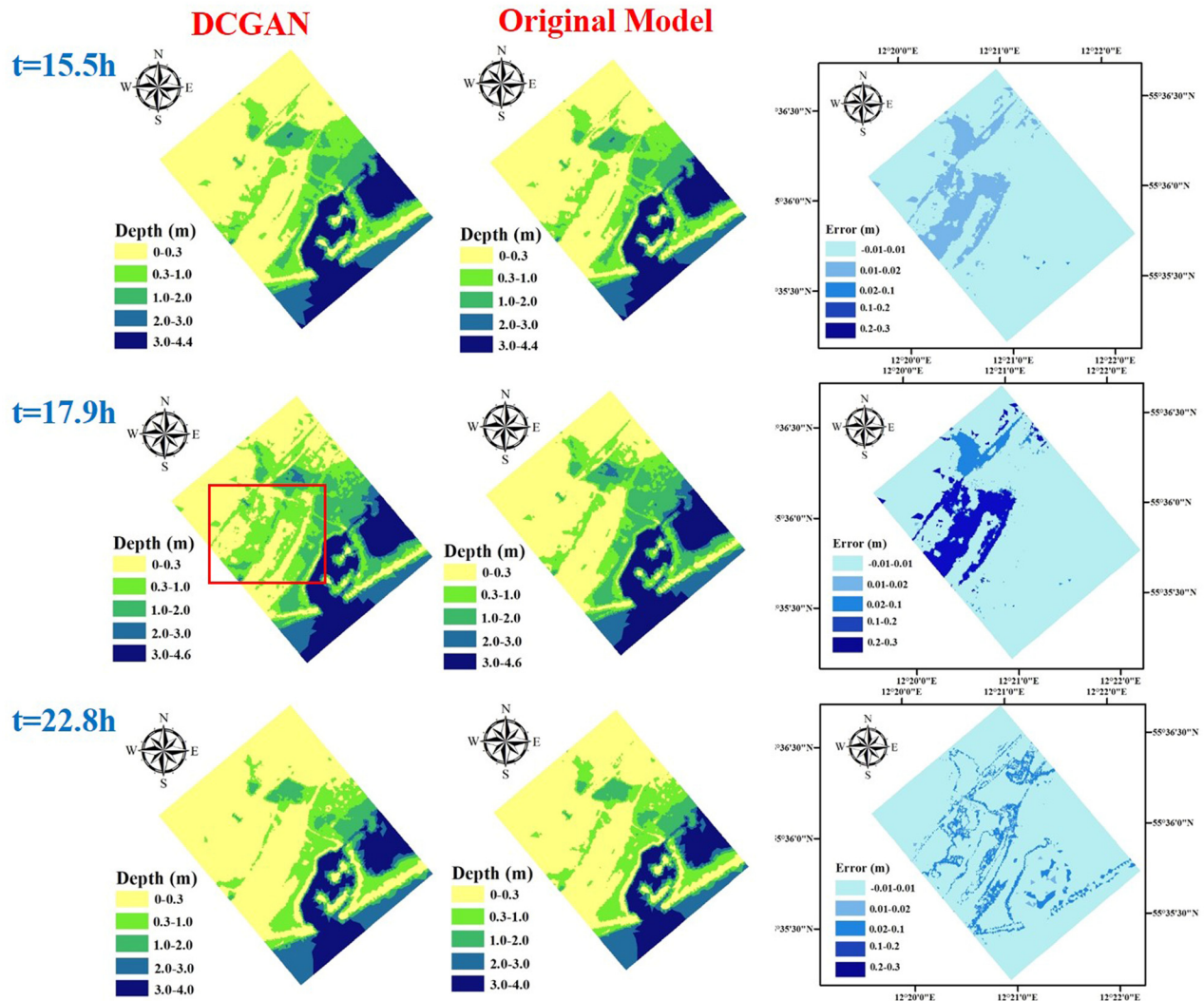
FIG. 10. Comparison of the spatial distribution of predictive water depth obtained from the DCGAN and the original high fidelity model at time steps $t = 15.5, 17.9, 22.8$ h.

$t = 18$ h. This suggests the flood forecasting accuracy is highly correlated with the incoming waves, which exhibits a descending trend when the water level of the incoming wave increases. It is also noted that the forecast reliability diminishes after $t = 21$ h. The reason for this is that the forecasting results have a smaller inundation as the incoming wave decays after $t = 21$ h, and the water depth in most parts of study area decreases to some extent, and may even reach dry conditions. Again, it proves that the flood forecasting accuracy is sensitive to the boundary conditions, i.e., the incoming sea level.[43]

In Fig. 11, we can see that there is no obvious trend of increasing forecast error with rising the lead-time while the statistical error analysis exhibits a close connection with incoming waves. One of the reasons for this is the inclusion of boundary conditions in the inputs at each predictive time step. The use of the boundary conditions (acting as the flood event driver) in the DCGAN, could improve the flood predictions at long lead-time series and mitigate the cumulated forecast error problem. This finding is similar to that of Ref. 47, where authors found that the driven variables included in weather forecast patterns could achieve higher accuracies and longer lead-time prediction with use of deep learning methods. While the inclusion of boundary conditions in deep learning leads to a better model performance,[48] there is often a lack of information on boundary conditions in a realistic application. To tackle this issue, inverse uncertainty quantification techniques can be used for estimation and calibration of boundary conditions. The boundary conditions for limited area simulations (LAS) are usually obtained from a global model or a large-scale model containing the area of LAS.

Overall, the results obtained suggest that the DCGAN is a powerful tool in flow pattern generalization and in nonlinear flow forecasting beyond the training period. In future research work, the trained
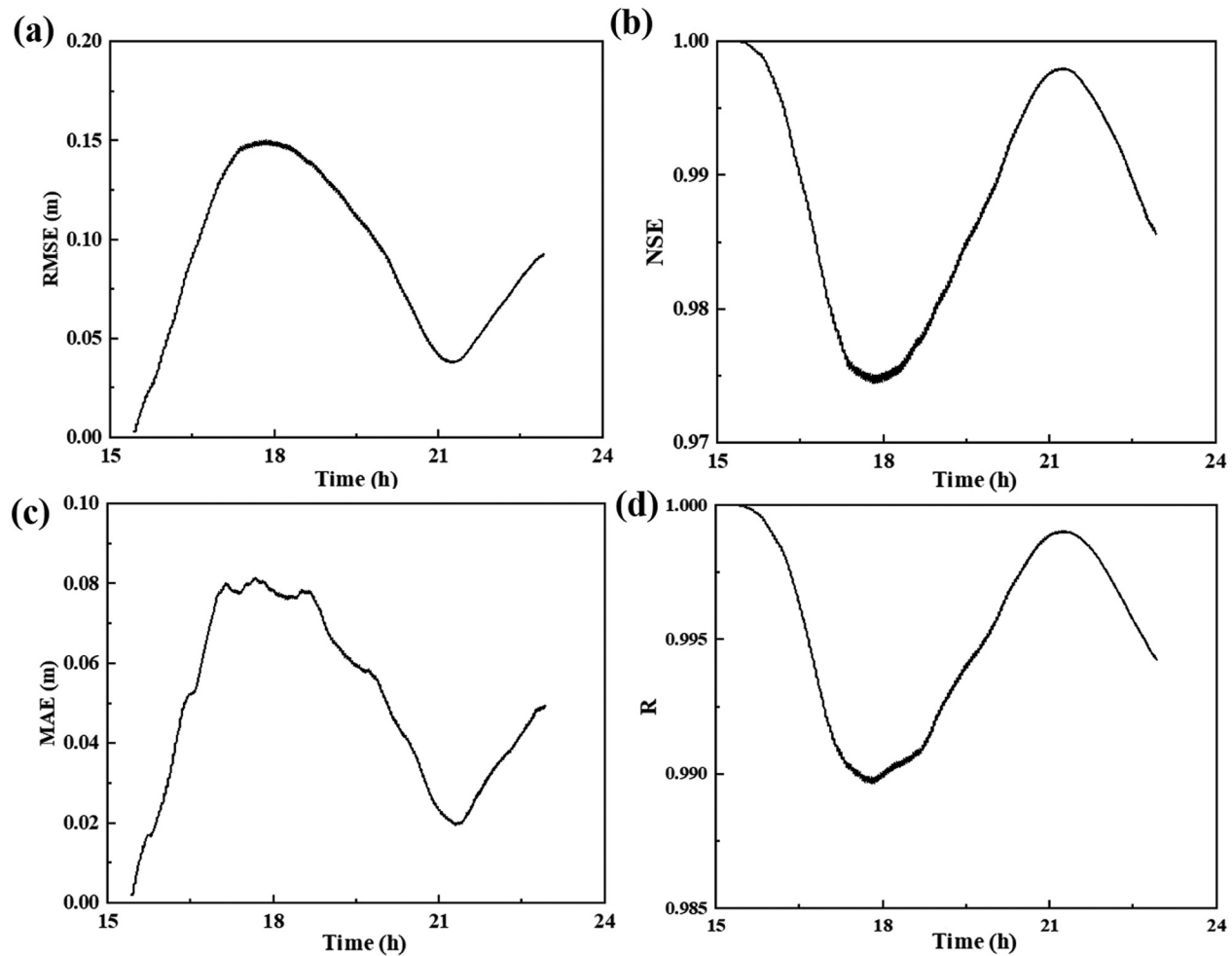
FIG. 11. Forecast performance with the DCGAN during the long lead-time of the computational domain area Ω: (a) RMSE, (b) NSE, (c) MAE, and (d) R.

DCGAN could also be incorporated into data assimilation techniques, which can effectively improve the predictive accuracy along with the real-time driving forcing.[49]

V. CONCLUSION

Real-time forecasting is of great significance for better decision-making in flood disasters. In this work, a real-time DCGAN predictive modeling tool for flood forecasting has been developed. This tool has the capabilities of dynamic learning and real-time forecast. The DCGAN can be used to compress the high-dimensional flood fields into the low-dimensional features, and then recover these latent states into the original ones. This process extracts the fluid flow features and learns the dynamic flow patterns.

The proposed approach is assessed with two scenarios, one focuses on uncertainty quantification of inflow boundary conditions and the other on evaluation of long lead-time predictive performance of the DCGAN tool. It has been applied to flood events within Greve, Denmark. The results show that the DCGAN is able to capture the complex flow features and explore the flood propagation process over the urban area. It exhibits an overall good agreement with the original high fidelity model in simulations of spatiotemporal flow distribution for a lead-900 time step forecast.

Overall, the proposed tool enables rapid and accurate long lead-time forecast of dynamic flows and has great potential for real-time forecasting and management, e.g., flood hazard mitigation and advanced management of policy responses to flood disaster, effective water resource management, and irrigation management decisions. In future work, the DCGAN performance for a long lead-time forecast will be further evaluated in other real applications (e.g., pollution forecast). The capability of other advanced deep learning methods (e.g., convolutional-LSTM[22]) for real-time forecasting will be also explored. Data assimilation techniques will be introduced to deep learning for improving the model accuracy.

ACKNOWLEDGMENTS

DATA AVAILABILITY

The data that support the findings of this study are available from the corresponding author upon reasonable request.

REFERENCES

[1] POST, "Urban flooding," Technical Report No. 289, 2007.

[2] Y.-G. Ham, J.-H. Kim, and J.-J. Luo, "Deep learning for multi-year ENSO forecasts," Nature **573**, 568–572 (2019).

[3] W.-c. Wang, K.-w. Chau, L. Qiu, and Y.-b. Chen, "Improving forecasting accuracy of medium and long-term runoff using artificial neural network based on EEMD decomposition," Environ. Res. **139**, 46–54 (2015).

[4] G. Bontempi and S. B. Taieb, "Conditionally dependent strategies for multiple-step-ahead prediction in local learning," Int. J. Forecast. **27**, 689–699 (2011).

[5] Z. M. Yaseen, A. El-Shafie, O. Jaafar, H. A. Afan, and K. N. Sayl, "Artificial intelligence based models for stream-flow forecasting: 2000–2015," J. Hydrol. **530**, 829–844 (2015).

[6] A. Farajpour, H. Farokhi, M. H. Ghayesh, and S. Hussain, "Nonlinear mechanics of nanotubes conveying fluid," Int. J. Eng. Sci. **133**, 132–143 (2018).

[7] H. Dai, A. Abdelkefi, and L. Wang, "Modeling and nonlinear dynamics of fluid-conveying risers under hybrid excitations," Int. J. Eng. Sci. **81**, 1–14 (2014).

[8] G. Bontempi, S. B. Taieb, and Y.-A. Le Borgne, "Machine learning strategies for time series forecasting," in European Business Intelligence Summer School (Springer, 2012), pp. 62–77.

[9] M. Reichstein, G. Camps-Valls, B. Stevens, M. Jung, J. Denzler, N. Carvalhais et al., "Deep learning and process understanding for data-driven earth system science," Nature **566**, 195–204 (2019).

[10] S. Pawar, O. San, B. Aksoylu, A. Rasheed, and T. Kvamsdal, "Physics guided machine learning using simplified theories," Phys. Fluids **33**, 011701 (2021).

[11] F. Hadavimoghaddam, M. Ostadhassan, E. Heidaryan, M. A. Sadri, I. Chapanova, E. Popov, A. Cheremisin, and S. Rafieepour, "Prediction of dead oil viscosity: Machine learning vs. classical correlations," Energies **14**, 930 (2021).

[12] S. Sahoo, T. A. Russo, J. Elliott, and I. Foster, "Machine learning algorithms for modeling groundwater level changes in agricultural regions of the us," Water Resour. Res. **53**, 3878–3895, https://doi.org/10.1002/2016WR019933 (2017).

[13] Y. LeCun, Y. Bengio, and G. Hinton, "Deep learning," Nature **521**, 436–444 (2015).

[14] S. Wiewel, M. Becher, and N. Thuerey, "Latent space physics: Towards learning the temporal evolution of fluid flow," in Computer Graphics Forum, Vol. 38 (Wiley Online Library, 2019), pp. 71–82.

[15] M. Cheng, F. Fang, T. Kinouchi, I. Navon, and C. Pain, "Long lead-time daily and monthly streamflow forecasting using machine learning methods," J. Hydrol. **590**, 125376 (2020).

[16] Y. Yin, P. Yang, Y. Zhang, H. Chen, and S. Fu, "Feature selection and processing of turbulence modeling based on an artificial neural network," Phys. Fluids **32**, 105117 (2020).

[17] S. Pawar, S. E. Ahmed, O. San, and A. Rasheed, "Data-driven recovery of hidden physics in reduced order modeling of fluid flows," Phys. Fluids **32**, 036602 (2020).

[18] R. Hu, F. Fang, C. C. Pain, and I. M. Navon, "Rapid spatio-temporal flood prediction and uncertainty quantification using a deep learning method," J. Hydrol. **575**, 911 (2019).

[19] X. Shi, Z. Chen, H. Wang, D.-Y. Yeung, W.-k. Wong, and W.-c. Woo, "Deep learning for precipitation nowcasting: A benchmark and a new model," in Advances in Neural Information Processing Systems, edited by C. Cortes, N.

[20] Lawrence, D. Lee, M. Sugiyama, and R. Garnett (Curran Associates, Inc., 2017), Vol. 30, pp. 5617–5627.

[20] R. Han, Y. Wang, Y. Zhang, and G. Chen, "A novel spatial-temporal prediction method for unsteady wake flows based on hybrid deep neural network," Phys. Fluids **31**, 127101 (2019).

[21] S. E. Ahmed, S. M. Rahman, O. San, A. Rasheed, and I. M. Navon, "Memory embedded non-intrusive reduced order modeling of non-ergodic flows," Phys. Fluids **31**, 126602 (2019).

[22] X. Shi, Z. Chen, H. Wang, D.-Y. Yeung, W.-k. Wong, and W.-c. Woo, "Convolutional LSTM network: A machine learning approach for precipitation nowcasting," in Advances in Neural Information Processing Systems, edited by C. Cortes, N. Lawrence, D. Lee, M. Sugiyama, and R. Garnett (Curran Associates, Inc., 2015), Vol. 28, pp. 802–810.

[23] Z. M. Yaseen, M. F. Allawi, A. A. Yousif, O. Jaafar, F. M. Hamzah, and A. El-Shafie, "Non-tuned machine learning approach for hydrological time series forecasting," Neural Comput. Appl. **30**, 1479–1491 (2018).

[24] O. Prakash, K. Sudheer, and K. Srinivasan, "Improved higher lead time river flow forecasts using sequential neural network with error updating," J. Hydrol. Hydromech. **62**, 60–74 (2014).

[25] C.-L. Huang, N.-S. Hsu, and C.-C. Wei, "Coupled heuristic prediction of long lead-time accumulated total inflow of a reservoir during typhoons using deterministic recurrent and fuzzy inference-based neural network," Water **7**, 6516–6550 (2015).

[26] P. Bento, J. Pombo, R. Mendes, M. Calado, and S. Mariano, "Ocean wave energy forecasting using optimised deep learning neural networks," Ocean Eng. **219**, 108372 (2021).

[27] S. Fan, N. Xiao, and S. Dong, "A novel model to predict significant wave height based on long short-term memory network," Ocean Eng. **205**, 107298 (2020).

[28] T. Liu, K. de Haan, Y. Rivenson, Z. Wei, X. Zeng, Y. Zhang, and A. Ozcan, "Deep learning-based super-resolution in coherent imaging systems," Sci. Rep. **9**, 3926 (2019).

[29] C. Ledig, L. Theis, F. Huszár, J. Caballero, A. Cunningham, A. Acosta, A. Aitken, A. Tejani, J. Totz, Z. Wang et al., "Photo-realistic single image super-resolution using a generative adversarial network," in Proceedings of the IEEE Conference on Computer Vision and Pattern Recognition (2017), pp. 4681–4690.

[30] Y. Choi, M. Choi, M. Kim, J.-W. Ha, S. Kim, and J. Choo, "StarGAN: Unified generative adversarial networks for multi-domain image-to-image translation," in Proceedings of the IEEE Conference on Computer Vision and Pattern Recognition (2018), pp. 8789–8797.

[31] P. Isola, J.-Y. Zhu, T. Zhou, and A. A. Efros, "Image-to-image translation with conditional adversarial networks," in Proceedings of the IEEE Conference on Computer Vision and Pattern Recognition (2017), pp. 1125–1134.

[32] N. Gao, H. Xue, W. Shao, S. Zhao, K. K. Qin, A. Prabowo, M. S. Rahaman, and F. D. Salim, Generative adversarial networks for spatio-temporal data: A survey" arXiv:2008.08903 (2020).

[33] M. Cheng, F. Fang, C. C. Pain, and I. M. Navon, "Data-driven modelling of nonlinear spatio-temporal fluid flows using a deep convolutional generative adversarial network," Comput. Methods Appl. Mech. Eng. **365**, 113000 (2020).

[34] I. Goodfellow, J. Pouget-Abadie, M. Mirza, B. Xu, D. Warde-Farley, S. Ozair, A. Courville, and Y. Bengio, "Generative adversarial nets," in Advances in Neural Information Processing Systems (Curran Associates, Inc., 2014), pp. 2672–2680.

[35] Z. Zhong, A. Y. Sun, and H. Jeong, "Predicting CO_2 plume migration in heterogeneous formations using conditional deep convolutional generative adversarial network," Water Resour. Res. **55**, 5830–5851, https://doi.org/10.1029/2018WR024592 (2019).

[36] J. A. Weyn, D. R. Durran, and R. Caruana, "Improving data-driven global weather prediction using deep convolutional neural networks on a cubed sphere," J. Adv. Model. Earth Syst. **12**, e2020MS002109 (2020).

[37] S. Ioffe and C. Szegedy, "Batch normalization: Accelerating deep network training by reducing internal covariate shift," in International Conference on Machine Learning (PMLR, 2015), pp. 448–456.

[38] D. P. Kingma and J. Ba, "Adam: A method for stochastic optimization," arXiv:1412.6980 (2014).

[39]T. Tieleman and G. Hinton, "RMSprop: Divide the gradient by a running average of its recent magnitude," COURSERA: Neural Networks for Machine Learning (2012).

[40]E. Heidaryan, "A note on model selection based on the percentage of accuracy-precision," J. Energy Resour. Technol. **141**, 045501 (2019).

[41]X. Xu, X. Zhang, H. Fang, R. Lai, Y. Zhang, L. Huang, and X. Liu, "A real-time probabilistic channel flood-forecasting model based on the Bayesian particle filter approach," Environ. Modell. Software **88**, 151–167 (2017).

[42]S. Berbel Roman, "Modelling flooding from the sea interacting with the drainage system under the influence of combined flood hazards to develop risk management strategies for the coastal region of Greve, Denmark," Master's thesis (University of Nice Sophia Antipolis, Nice, France, 2014).

[43]R. Hu, F. Fang, P. Salinas, C. Pain, N. S. Domingo, and O. Mark, "Numerical simulation of floods from multiple sources using an adaptive anisotropic unstructured mesh method," Adv. Water Resour. **123**, 173–188 (2019).

[44]DHI MIKE21 and F. MIKE3 Flow Model, "*Hydrodynamic and transport module scientific documentation,*" DHl Water and Environment, Denmark, 2009.

[45]J. Leinonen, A. Guillaume, and T. Yuan, "Reconstruction of cloud vertical structure with a generative adversarial network," Geophys. Res. Lett. **46**, 7035–7044, https://doi.org/10.1029/2019GL082532 (2019).

[46]Z. Li, M.-A. Meier, E. Hauksson, Z. Zhan, and J. Andrews, "Machine learning seismic wave discrimination: Application to earthquake early warning," Geophys. Res. Lett. **45**, 4773–4779, https://doi.org/10.1029/2018GL077870 (2018).

[47]A. Chattopadhyay, E. Nabizadeh, and P. Hassanzadeh, "Analog forecasting of extreme-causing weather patterns using deep learning," J. Adv. Model. Earth Syst. **12**, e2019MS001958 (2020).

[48]M.-A. Boucher, J. Quilty, and J. Adamowski, "Data assimilation for streamflow forecasting using extreme learning machines and multilayer perceptrons," Water Resour. Res. **56**, e2019WR026226, https://doi.org/10.1029/2019WR026226 (2020).

[49]C. Irrgang, J. Saynisch-Wagner, and M. Thomas, "Machine learning-based prediction of spatiotemporal uncertainties in global wind velocity reanalyses," J. Adv. Model. Earth Syst. **12**, e2019MS001876 (2020).